

# Rapid Automated Three-Dimensional Tracing of Neurons From Confocal Image Stacks

Khalid A. Al-Kofahi, Sharie Lasek, Donald H. Szarowski, Christopher J. Pace, George Nagy, *Senior Member, IEEE*, James N. Turner, and Badrinath Roysam, *Member, IEEE*

**Abstract**—Algorithms are presented for fully automatic three-dimensional (3-D) tracing of neurons that are imaged by fluorescence confocal microscopy. Unlike previous voxel-based skeletonization methods, the present approach works by recursively following the neuronal topology, using a set of  $4 \times N^2$  directional kernels (e.g.,  $N = 32$ ), guided by a generalized 3-D cylinder model. This method extends our prior work on exploratory tracing of retinal vasculature to 3-D space. Since the centerlines are of primary interest, the 3-D extension can be accomplished by four rather than six sets of kernels. Additional modifications, such as dynamic adaptation of the correlation kernels, and adaptive step size estimation, were introduced for achieving robustness to photon noise, varying contrast, and apparent discontinuity and/or hollowness of structures. The end product is a labeling of all somas present, graph-theoretic representations of all dendritic/axonal structures, and image statistics such as soma volume and centroid, soma interconnectivity, the longest branch, and lengths of all graph branches originating from a soma. This method is able to work directly with unprocessed confocal images, without expensive deconvolution or other preprocessing. It is much faster than skeletonization, typically consuming less than a minute to trace a 70-MB image on a 500-MHz computer. These properties make it attractive for large-scale automated tissue studies that require rapid on-line image analysis, such as high-throughput neurobiology/angiogenesis assays, and initiatives such as the Human Brain Project.

**Index Terms**—Automated morphometry, micrograph analysis, neuron tracing, three-dimensional (3-D) image filtering, three-dimensional (3-D) vectorization.

## I. INTRODUCTION

THE quantitative morphology of linear branched structures such as blood vessels and neurons is of broad interest [1]–[7]. Of particular interest is the automated three-dimensional (3-D) tracing and morphometry of neurons in thick slices of brain tissue, imaged by 3-D microscopy [8]–[11]. Fig. 1 presents the projections onto the  $x$ - $y$ ,  $x$ - $z$ , and  $y$ - $z$  planes

Manuscript received April 4, 2000; revised June 22, 2001 and August 22, 2001.

K. A. Al-Kofahi and G. Nagy are with the Electrical, Computer, and Systems Engineering Department, Rensselaer Polytechnic Institute, Troy, NY 12180-3590 USA (e-mail: roysam@ccse.rpi.edu).

J. N. Turner is with the Biomedical Engineering Department, Rensselaer Polytechnic Institute, Troy, NY 12180-3590 USA.

S. Lasek, D. H. Szarowski, and J. N. Turner are with the Wadsworth Center, NY State Department of Health, Albany, NY 12201-0509 USA.

C. J. Pace is with the Department of Biology, The State University of New York at Albany, Albany, NY 12201 USA.

B. Roysam is with the Electrical, Computer, and Systems Engineering Department, Rensselaer Polytechnic Institute, Troy, NY 12180-3590 USA and is also with the Biomedical Engineering Department, Rensselaer Polytechnic Institute, Troy, NY 12180-3590 USA.

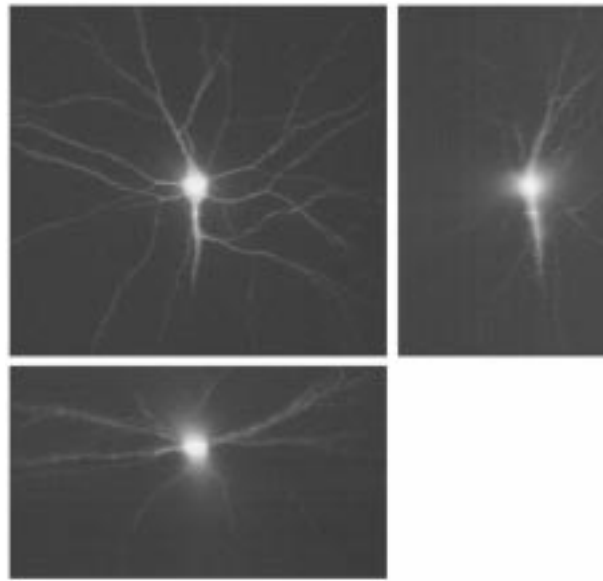
Publisher Item Identifier S 1089-7771(02)05310-4.

of a sample 3-D image of a selectively stained neuron. The image has dimensions  $512 \times 480 \times 301$  pixels with a depth of 8 bits/pixel (70 Mbytes). It is desired to trace the dendrites and axon, and produce a graph-theoretic or tabular representation that captures the essential topological characteristics. It is also of interest to segment the soma (cell body) and relate the traces to the soma. A number of topological and metric measurements could then be made [1].

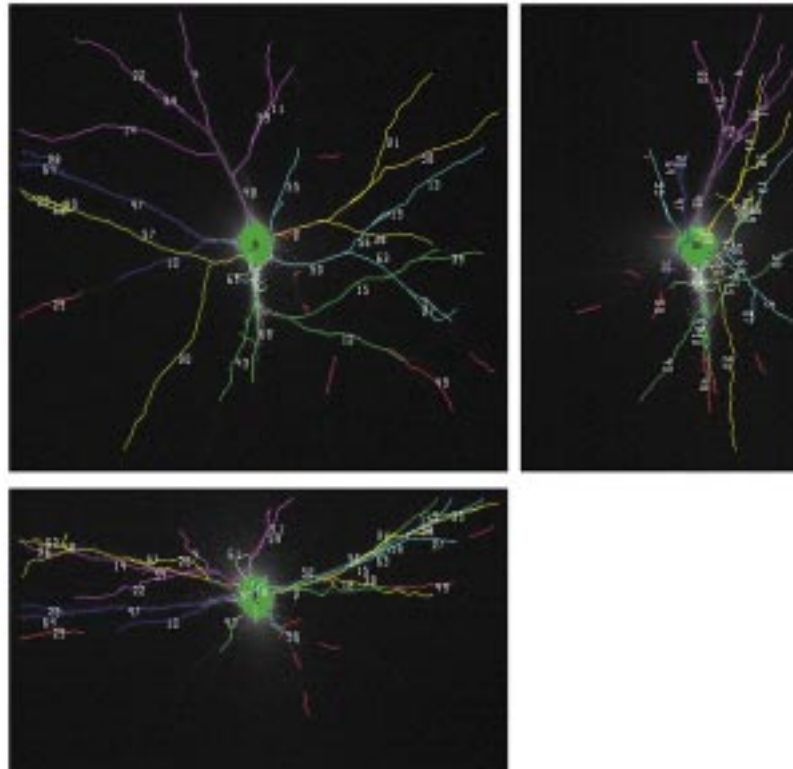
Capowski [1] has provided a detailed history of neuron tracing methods. Briefly, current methods are semiautomatic. A human interacts with a microscope enhanced with computer imaging hardware and software [14]. The user performs pattern recognition. The computer system records the data and generates topological and metric analyses. In some cases, the computer assists the human by automatically aligning a cursor to the nearest image feature or by automatically focusing the microscope [1], [12]–[14]. Cohen *et al.* [15] presented a method for automatic 3-D tracing from confocal image stacks of selectively stained neurons based on segmentation, skeletonization, and graph extraction. Their work has been refined by He *et al.* [16], [17]. The new algorithms presented here are inspired by methods that we developed for tracing vasculature in retinal angiograms [18], [34]. They are superior in terms of speed, automation, and robustness compared to skeletonization-based methods for tracing neuronal structure. If smaller structures such as spines are also of interest, skeletonization can still be employed on a localized basis.

## II. IMAGE ANALYSIS BACKGROUND

Three approaches exist for analysis of linear branched structures such as neurons and vasculature. The first is based on skeletonization and branch point analysis (e.g., [15], [19]–[23]). The second is based on enhancing edge/line properties and then identifying vessel contours by chaining edge pixels together. Such a chaining process usually involves dynamic programming to search for a minimum cost path, Markov chaining, or maximizing the likelihood of a path [24]–[31]. Both approaches require the processing of every image pixel with numerous operations per pixel, hence, they tend to scale poorly with image size. Cohen *et al.* [15] described methods to reduce the computational effort by processing only the foreground pixels selected by a segmentation operation. Nevertheless, 3-D skeletonization is computationally intensive. The third approach, exemplified by this paper and others, is referred to variously as vectorization, vectorial tracking, or tracing [18], [23], [32], [33]. These methods first locate an initial point,



(a)



(b)

Fig. 1. (a) Sample  $512 \times 480 \times 301$  image of a dye-injected neuron in a thick brain slice, presented by its projections ( $x$ - $y$ ,  $y$ - $z$ , and  $x$ - $z$ ). The axial step size is  $0.5 \mu\text{m}$ , and the zoom factor is 1.0. (b) The tracing result. Each tree emanating from the soma is labeled with a unique color. A unique number identifies each segment. These numbers are correlated with the text output (Fig.8c). The color red is reserved for segments not connected to a soma (e.g., 52, lower right). Intersection, branching, and starting points are indicated by blue dots.

and then exploit local image properties to trace the structures recursively. They process only pixels close to the structures and so are appropriately termed “exploratory algorithms” They are particularly appropriate when processing speed is crucial, such as in real-time image analysis [18], [34], or when the data sets are very large.

Broadly, three categories of exploratory processing techniques are described in the literature. In the first, commonly

used in quantitative coronary angiography (QCA), the initial and end points of a vessel (sometimes also an initial centerline) are entered manually [24]–[26], [28], [35]–[43]. Although very accurate, these algorithms are designed to trace vessel segments with no branching or intersections, and speed is not a concern. In the second category, the algorithm starts with a manually entered initial point and an initial direction, and recursively traces the entire arterial tree [44], [45] using a breadth-first

search. In the context of neurons, this would correspond to tracing a single axon/dendrite tree that is efferent from a single soma. Such methods are not suitable for images containing several neurons with each neuron having several processes efferent from it, and when neurons are larger than the field of view. The third category consists of fully automated methods [18] that overcome the limitations of the first two.

The bulk of the prior literature on vectorization is concerned with two-dimensional (2-D) images, or projections of 3-D images [32], [37], [42], [43], [47], [48]. The method presented here extends the prior work, especially [18], to handle 3-D (volumetric) data. A second contribution of the present work is a set of adaptations to handle the imaging artifacts prevalent in fluorescence confocal microscope images, especially noise, the point-spread function, and discontinuities in structures.

### III. METHODS

The images are acquired using a laser-scanning confocal microscope [49], [50]. This instrument scans thick (compared to the depth of field) specimens in successive layers. The 3-D imaging can also be accomplished by deconvolution of through-focus series from standard wide-field microscopes [10], but generally not from such thick objects. The end result in either case is a 3-D array of volumetric optical intensity measurements. Typical imaging artifacts encountered include variable quantum noise, point spread, signal attenuation with depth, and nonuniformity of staining causing apparent discontinuity in structures [49].

The large size of 3-D confocal images (50–100 MB) is a challenge. Even a modest operation can entail excessive computation if repeated at each voxel. This problem is circumvented by avoiding operations that process each voxel. An adaptive exploratory search of the image is conducted, directly at the voxel intensity level. This limits computations to just the sparse structures of interest and, therefore, scales with the complexity of the neurons rather than image size. The resulting algorithms are highly adaptive since they rely on local image information. This is crucial since biological images are inherently variable.

Sections III-A–F describe the algorithms for tracing the dendrites/axons, segmenting the soma, and generating a complete graph-theoretic representation of the neuron.

#### A. A Generalized Cylinder Model of the Neuronal Structures

Over a short distance, the dendrites and axons in the image field are well approximated by generalized cylinders, i.e., cylinders with elliptical cross sections, and some curvature along the axis. The nature of the confocal imaging process usually implies that the images are nonisotropic, with maximum separation along the optical axis of the microscope, so the principal axes of the generalized cylinder are aligned with the  $x$ - $y$  plane and/or the optical axis. This implies that it is sufficient to sample these ellipses along just two, instead of three directions. The results shown in this paper demonstrate that this approximation does not result in serious limitations.

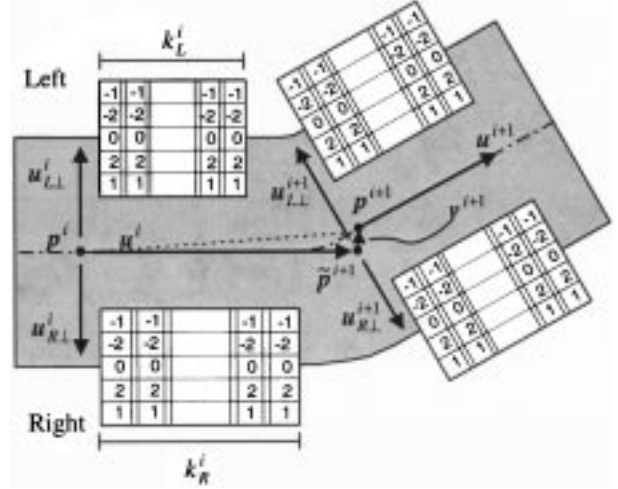


Fig. 2. Illustrating the 2-D tracing algorithm. Starting from centerline point  $\mathbf{p}^i$ , and initial direction  $\mathbf{u}^i$  the perpendicular directions  $\mathbf{u}_{L\perp}^i$  and  $\mathbf{u}_{R\perp}^i$  are searched for the left and right boundaries, where the correlation responses are maximal. A step is taken along the direction of maximal response to  $\mathbf{p}^{i+1}$ . This is corrected by vector  $\mathbf{v}^{i+1}$  to the next centerline point  $\mathbf{p}^{i+1}$ . The next tracing direction  $\mathbf{u}^{i+1}$  is a weighted average combining  $\mathbf{u}^i$  and the directions of the maximal-response kernels at step  $i + 1$ . The kernel lengths  $k_R^i$  and  $k_L^i$  are set adaptively and can be different.

#### B. Directional Matched Low-Pass Differentiator Kernels for Generalized Cylinders

The rest of this section provides a detailed description of the algorithms. Nonmathematical readers may prefer to skim or skip this material entirely. Table II summarizes the notation.

The 2-D tracing algorithms described in prior work [18], [37], [44] used a set of correlation kernels of the form  $[-1, -2, 0, 2, 1]^T$  perpendicular to the structures being traced and computed a moving average along their length. These kernels are illustrated in Fig. 2, for the case when the moving average is computed over  $K$  pixels. The  $5 \times K$  kernel is referred to as a “template” in our work. Separate templates are constructed for application at the left and right boundaries of the structures and along different orientations. The possible orientations are discretized to a small number of values; typically 16 or 32. As illustrated in Fig. 2, the template whose axis coincides with the boundary of the structure being traced produces the highest correlation response. These maximal responses guide the tracing, using an update equation of the form

$$\mathbf{p}^{i+1} = \mathbf{p}^i + \alpha^i \mathbf{u}^i \quad (1)$$

where  $\alpha$  is a step size [18]. The above update equation produces nonsmooth traces, especially when the local curvature is high. As illustrated in Fig. 2, smoother traces are obtained by adding a fine-tuning step to (1), resulting in the following update equations:

$$\tilde{\mathbf{p}}^{i+1} = \mathbf{p}^i + \alpha^i \mathbf{u}^i \quad (2a)$$

$$\mathbf{p}^{i+1} = \tilde{\mathbf{p}}^{i+1} + \mathbf{v}^{i+1} \quad (2b)$$

where  $\mathbf{v}^{i+1}$  is a correction (fine-tuning) vector, and “ $\sim$ ” indicates approximation. An extension of the templates to 3-D space is illustrated in Fig. 3(a). Analogous to the 2-D case, the templates are applied along the length of the structure being traced.

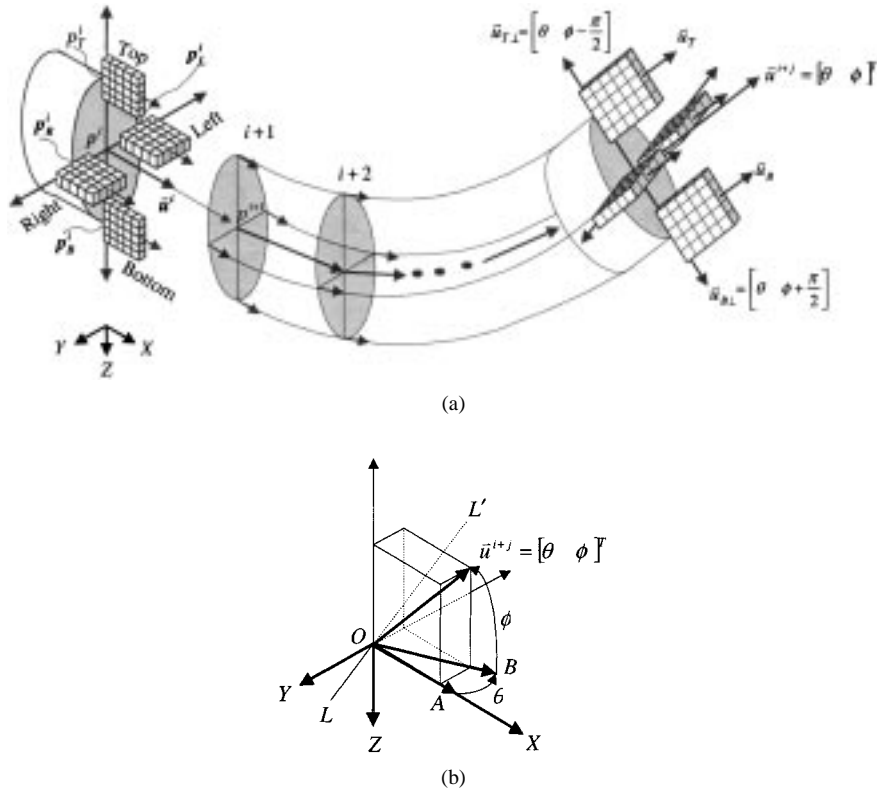


Fig. 3. Illustrating the 3-D tracing algorithm. (a) Four sets of kernels are used, instead of two. Starting from point  $\mathbf{p}^{i+1}$ , the left, right, top, and bottom boundary points,  $\mathbf{p}_L^i$ ,  $\mathbf{p}_R^i$ ,  $\mathbf{p}_T^i$ , and  $\mathbf{p}_B^i$ , are detected. The response of each kernel is computed in  $N \times N$  angular directions. The directions of the strongest kernel responses are used to estimate the local centerline direction  $\bar{\mathbf{u}}^i$  along which to take a step. The right-hand portion of (a) illustrates the notation used in the text. (b) The coordinate system for specifying angular directions. A unit vector  $\mathbf{u}^{i+j}$ , also illustrated on the right-hand part of (a), is obtained by rotating the vector  $OA$  by  $\theta^\circ$  relative to the  $x$  axis in the  $x$ - $y$  plane, and then rotating the resulting vector (i.e.,  $OB$ ) by  $\phi^\circ$  relative to the  $x$ - $y$  plane.

The third dimension is sampled in two perpendicular planes, keeping in mind the generalized cylinder model described earlier. Four sets of templates, labeled “right,” “left,” “top,” and “bottom,” respectively, are defined. Similar to the 2-D case, the templates most closely oriented along the generalized cylinder, and centered on the boundary produce a maximum response. This fact is exploited to conduct the tracing.

Directions in 3-D space are described in terms of two angles,  $\theta$  and  $\phi$ . As illustrated in Fig. 3(b),  $\theta$  describes a rotation around the  $Z$  axis, and  $\phi$  describes a rotation around the line  $LL'$  (i.e., the  $Y$  axis after being rotated by  $\theta^\circ$  around the  $Z$  axis). Note that the angular directions in the coordinate system shown in Fig. 3(b) follow the *right-hand* rule. Both  $\theta$  and  $\phi$  are discretized to  $N$  values each, resulting in a total of  $N \times N$  angular directions. The value of  $N$  can be set by the user to best sample the curvature of the structures of interest. For the experimental results presented here, we used  $N = 32$  yielding an angular precision of  $11.25^\circ$  and a total of  $N^2 = 1024$  unique directions. The total number of unique templates taking into account the four sets (right, left, top, and bottom) is therefore  $4 \times N^2 = 4096$ . It is convenient to refer to each of the discrete angular orientations by integer indexes  $s_1$  and  $s_2$ , with  $s_1$  and  $s_2 \in \{0, \dots, N-1\}$ . A unit vector  $\mathbf{u}$  with the orientation  $[\theta = 2\pi s_1/N, \phi = 2\pi s_2/N]$  is expressed as  $\mathbf{u} = [s_1, s_2]^T$ . For example, a unit vector along the  $x$ -axis, i.e., a vector with angles  $\theta = 0^\circ$ , and  $\phi = 0^\circ$  is expressed concisely as  $\mathbf{u}_x = [0, 0]^T$ . With the above notation, a template is specified by its orientation, denoted  $\mathbf{u} = [s_1, s_2]^T$ , a perpendicular shift direction, denoted  $\mathbf{u}_\perp$ , and its length  $k$ . The perpendicular direction  $\mathbf{u}_\perp$  is the line along which the templates

are correlated repeatedly to search for boundaries. These directions are illustrated in the right-hand part of Fig. 3(a).

In our prior work with retinal images [18], the templates were of fixed length,  $k = 6$ . For the present work, the length is allowed to vary. Longer templates perform more averaging along the structures, and are necessary to trace the noisier and discontinuous structures encountered in confocal neuron images. On the other hand, longer templates are unsuitable for tracing highly tortuous structures. The number of angular quantization levels  $N$  imposes a lower bound on the value of template's length  $k$  according to

$$k \geq \left\lceil \frac{1}{\sin\left(\frac{2\pi}{N}\right)} \right\rceil. \quad (3)$$

At equality, templates along adjacent directions differ by at most one voxel at their far end. Based on these considerations, the template length was allowed to vary between 8 and 50 in the present work. The method for selecting the optimal value of  $k$  adaptively, at each tracing step, is described in Section III-C.

As in prior 2-D work, the templates are correlated with the image. Let  $R(\mathbf{u}_R, k, \mathbf{p})$  denote the correlation response of a *right* template of length,  $k$ , and direction,  $\mathbf{u}_R$ , with the image data  $\mathbf{I}(x, y, z)$  when the template is centered at the image point  $\mathbf{p}(x, y, z)$ . Similarly, let  $L(\mathbf{u}_L, k, \mathbf{p})$ ,  $T(\mathbf{u}_T, k, \mathbf{p})$ , and  $B(\mathbf{u}_B, k, \mathbf{p})$  denote the responses of the *left*, *top*, and *bottom* templates, respectively. Henceforth, these quantities are collectively referred to as the “template responses.”

### C. Application of the Templates to 3-D Neuron Tracing

Fig. 3 illustrates the procedure for tracing a 3-D generalized cylinder structure. Starting from a point  $\mathbf{p}^i$  on the centerline, and an initial estimate of the direction  $\mathbf{u}^i$ , the structure is traced recursively, estimating successive points  $\mathbf{p}^{i+1}, \mathbf{p}^{i+2}, \dots$ , along the centerline. This is repeated until a stopping criterion (defined in Section II-D) is met. This procedure requires: 1) a collection of seed points along with initial directions; 2) a mechanism for recursive application of templates; and 3) criteria to stop tracing whenever a structure's end is reached or erroneous background traces are being pursued. The procedure for obtaining seed points automatically is described in Section III-E. We describe the tracing algorithm below.

For simplicity of presentation, we first describe the algorithm using templates of fixed length  $k$ . This restriction is relaxed later. Denote a seed point on or near a centerline as  $\tilde{\mathbf{p}}^i$ . Denote the initial estimate of the local direction as  $\tilde{\mathbf{u}}^i$ . The first step is to refine these estimates. This is accomplished by computing the responses of the *right*, *left*, *top*, and *bottom* templates along the four perpendicular shift directions using a *shift and correlate* procedure as in prior work [18]. Briefly, each template is placed at a series of locations and their correlation with the image is computed. By design, this value, also termed “response,” is maximum at abrupt changes in brightness.

The points along the above-mentioned directions that produce maximum template responses are estimated as the boundaries  $\{\mathbf{p}_R^i, \mathbf{p}_L^i, \mathbf{p}_T^i, \mathbf{p}_B^i\}$ . The orientations of the templates that produce this maximum response yield a set of local direction estimates  $\{\mathbf{u}_R^i, \mathbf{u}_L^i, \mathbf{u}_T^i, \mathbf{u}_B^i\}$  at the boundaries. For the top and bottom templates, this can be described mathematically as shown in (4) and (5) at the bottom of the page, where  $M$  is the maximum expected axon/dendrite diameter, and  $\Sigma$  is the set of all possible directions. The equations for the other two templates are analogous. For the experiments described here,  $M$  was estimated empirically as  $M = 24$ .

Let  $\hat{R}^i = R(\mathbf{u}_R^i, k, \mathbf{p}_R^i)$  denote the maximal response of the right template at the boundary point estimated by the above procedure. The notation for the other three template types is defined in an analogous manner. With this notation, the method to refine the location and direction estimates  $\tilde{\mathbf{p}}^i$  and  $\tilde{\mathbf{u}}^i$  can be described as follows:

$$\begin{aligned} \mathbf{p}^i &= [x^i, y^i, z^i]^T \\ &= \frac{\tilde{\mathbf{p}}^i}{2} + \left[ \frac{\hat{R}^i x_R^i + \hat{L}^i x_L^i}{2(\hat{R}^i + \hat{L}^i)}, \frac{\hat{R}^i y_R^i + \hat{L}^i y_L^i}{2(\hat{R}^i + \hat{L}^i)}, \frac{\hat{T}^i z_T^i + \hat{B}^i z_B^i}{2(\hat{T}^i + \hat{B}^i)} \right]^T \end{aligned} \quad (6)$$

$$\begin{aligned} \mathbf{u}^i &= [s_1^i, s_2^i]^T \\ &= \frac{\tilde{\mathbf{u}}^i}{2} + \left[ \frac{\hat{R}^i s_{1R}^i + \hat{L}^i s_{1L}^i}{2(\hat{R}^i + \hat{L}^i)}, \frac{\hat{T}^i s_{2T}^i + \hat{B}^i s_{2B}^i}{2(\hat{T}^i + \hat{B}^i)} \right]^T. \end{aligned} \quad (7)$$

Using these refined estimates for the location and direction of the current centerline point, the location and direction of the next centerline point are updated as follows:

$$\tilde{\mathbf{p}}^{i+1} = \mathbf{p}^i + \alpha^i \mathbf{u}^i \quad (8)$$

$$\tilde{\mathbf{u}}^{i+1} = \mathbf{u}^i. \quad (9)$$

The above computations can be reduced substantially. For instance, it is not necessary to correlate the templates at all  $M/2$  points at each iteration  $i$  since most structures are narrower than  $M$  voxels. Also, correlating the templates at all  $M/2$  points exposes the tracing algorithm to the risk of being confused by the boundaries of adjacent parallel structures as explained in [18]. Such problems are avoided by terminating the shift and correlate procedure using a carefully defined criterion. Following [18] the procedure is terminated when the maximum template response so far is larger than a fixed threshold and the current response falls below 20% of the maximum.

To further reduce the computations, note that it is unnecessary to compute the template responses for each of the  $N^2$ -possible directions since most structures of interest have limited curvature. With this in mind, the set  $\Sigma$  can be limited to a small number of directions that are adjacent to  $\tilde{\mathbf{u}}^i$ . This subset of direction vectors denoted  $\Sigma^i$  is given by

$$\Sigma^i = \left\{ \tilde{\mathbf{u}}^i + [\pm \partial s_1, \pm \partial s_2]^T \mid \partial s_1, \partial s_2 = 0, 1, \dots, \Delta \Sigma \right\} \quad (10)$$

where  $\Delta \Sigma$  is the maximum number of neighboring directions. In the present work, this value was allowed to adapt between 2 and 3, depending on the estimated noise level in the image and/or user-set preferences. Note that when  $\Delta \Sigma = 2$ , the set  $\Sigma^i$  contains only 25 directions, a substantial reduction compared to 1024 directions in  $\Sigma$ .

*Method for Dynamic Adaptation of Template Length:* Allowing the template length  $k$  to vary enables tracing past discontinuities and noisy segments while being able to handle curvature. With a variable-length template, it is important to normalize the template response by the length so that meaningful comparisons can be made. Without such normalization, it is not valid to estimate boundary points as those maximizing template responses, since longer templates tend to produce larger responses, even though the boundary of a particular dendrite/axon might coincide better with a shorter template. With this in mind, the *length-normalized template response* is defined as the response per unit length of a template. Incorporating this extension to (4), and also the constraint on directions described in (10) yields (11), shown at the bottom of the page, where  $u_{T\perp}$  is a function of  $u_T$  as defined in Table I and  $K$  is the maximum allowed template length. For the present work,  $K$  was empirically set to 50. The

$$(\mathbf{p}_T^i, \mathbf{u}_T^i) = \arg \max_{\{(\mathbf{p}, \mathbf{u}_T) \mid \mathbf{p} = \tilde{\mathbf{p}}^i + m \mathbf{u}_{T\perp}, m = 1, \dots, M/2, \text{ and } \mathbf{u}_T \in \Sigma\}} T(\mathbf{u}_T, k, \mathbf{p}) \quad (4)$$

$$(\mathbf{p}_B^i, \mathbf{u}_B^i) = \arg \max_{\{(\mathbf{p}, \mathbf{u}_B) \mid \mathbf{p} = \tilde{\mathbf{p}}^i + m \mathbf{u}_{B\perp}, m = 1, \dots, M/2, \text{ and } \mathbf{u}_B \in \Sigma\}} B(\mathbf{u}_B, k, \mathbf{p}) \quad (5)$$

TABLE I

SUMMARY OF THE PERPENDICULAR SHIFT DIRECTIONS FOR THE TEMPLATES. SEE THE RIGHT-HAND PORTION OF FIG. 3(A) FOR A GRAPHIC ILLUSTRATION

Template	Direction	Perpendicular Shift Direction
<i>Right</i>	$\mathbf{u}_R = [s_1, s_2]^T$	$\mathbf{u}_{R\perp} = \left[ s_1 + \frac{N}{4}, s_2 \right]^T$
<i>Left</i>	$\mathbf{u}_L = [s_1, s_2]^T$	$\mathbf{u}_{L\perp} = \left[ s_1 - \frac{N}{4}, s_2 \right]^T$
<i>Top</i>	$\mathbf{u}_T = [s_1, s_2]^T$	$\mathbf{u}_{T\perp} = \left[ s_1, s_2 - \frac{N}{4} \right]^T$
<i>Bottom</i>	$\mathbf{u}_B = [s_1, s_2]^T$	$\mathbf{u}_{B\perp} = \left[ s_1, s_2 + \frac{N}{4} \right]^T$

equations for the other three cases are analogous. Table II shows symbols used in this paper.

Finally, the tracing algorithm computes an approximation for the location and direction of the next centerline point according to (8) and (9). The step size  $\alpha$  [in (8)] is a function of the templates lengths and is determined according to

$$\alpha^i = \max \left\{ 3, \frac{1}{4} \min (k_R^i, k_L^i, k_T^i, k_B^i) \right\}. \quad (12)$$

This favors larger step sizes for straight segments where the longer templates fit well. Ideally,  $\alpha$  should also be a function of the noise level in the image, but we leave this for future work. Currently, the algorithm uses a step-size of three if the user indicates that the image has a low signal-to-noise-ratio (SNR).

#### D. Stopping Criteria

Tracing is terminated upon reaching the end of the traced segment or upon straying away from the segment into the background. This situation is expressed as *multiple consecutive violations* of the following conditions, as explained below.

- The sum of the four maximum template responses is larger than a threshold according to

$$\hat{R}^i + \hat{L}^i + \hat{T}^i + \hat{B}^i > 3C (k_R^i + k_L^i + k_T^i + k_B^i) \quad (13)$$

where  $C$  is the image contrast, as measured by the difference  $C = \gamma_F - \gamma_I$ , between the foreground and overall median intensities  $\gamma_F$  and  $\gamma_I$ , respectively. Notice that correlating a template of length  $k$  at a unit step edge yields  $3k$ , hence the constant 3 in (13)

- The average intensity of the traced structure is at least one gray level higher than that of the local background. This translates to requiring the maximum response of each of

the four templates to be larger than a threshold. For a *right* template this is expressed as  $\hat{R}^i > 3k_R^i$ . Conditions for other templates are analogous.

- The maximum template response at a boundary point should be  $a$  times larger than the response of a template applied at the same point orthogonal to the boundary and pointing into the interior of the segment. For a *right* template this can be expressed as

$$\hat{R}^i (\mathbf{u}_R^i, k_R^i, \mathbf{p}_R^i) > a \frac{k}{k + k_R^i} R (-\mathbf{u}_{R\perp}^i, k, \mathbf{p}_R^i) \quad (14)$$

where  $a$  is a sensitivity factor that effectively imposes a constraint on the uniformity of the interior of the traced segment and is set empirically to two. The value of the template length  $k$ , on the right side of (14), is estimated by the distance between the left and right boundaries  $\|\mathbf{p}_R^i - \mathbf{p}_L^i\|$ .

At each iteration  $i$ , each of the above conditions is tested, and the number of violations are counted. Tracing is stopped if the number of consecutive violations is larger than a threshold  $\Gamma$ . In the experiments reported here,  $\Gamma$  was set to three. The rationale for this criterion is to tolerate responses that are characteristic of the background as long as such responses are isolated events due to noise and image artifacts.

#### E. Seed-Point Selection

The seed-point selection mechanism must ensure that for every dendritic/axonal segment, the tracing algorithm is provided with a seed point on or near the centerline of the segment along with an initial direction. A seed point is used twice, once in the specified direction and a second time in the opposite direction. To ensure coverage, redundant seed points are generated. The seed-point selection mechanism is a two-step process. In the first step, a pool of seed-point candidates is generated, and in the second step, unfit candidates are eliminated. This eliminates unnecessary computation.

- Step 1) **Line Searches over a Coarse Grid:** The 3-D neuron image is projected onto the  $x$ - $y$  plane using maximum projection and a grid of  $N$  horizontal lines and  $M$  vertical lines are superimposed on the resulting 2-D image, denoted  $I_{xy}$ . Seed candidates are identified by performing a set of  $N + M$  line searches over the image  $I_{xy}$ . The distance between consecutive lines, i.e., the grid spacing,  $g$ , is set empirically to 20 pixels based on the observation that most dendrites and axons are narrower than 20 pixels. The gray-level values on each line are low-pass filtered using a one-dimensional (1-D) kernel of the form  $[0.25, 0.5, 0.25]^T$ . Seed point candidates are identified as local intensity maxima on each line using a 1-D neighborhood of  $g$  pixels. In addition to being

$$(\mathbf{p}_T^i, \mathbf{u}_T^i, k_T^i) = \underset{\{(\mathbf{p}, \mathbf{u}_T, k) | \mathbf{p} = \hat{\mathbf{p}}^i + m\mathbf{u}_{T\perp}, m=1, \dots, M/2, \mathbf{u}_T \in \Sigma^i, k=8, \dots, K\}}{\arg \max} \left\{ \frac{T(\mathbf{u}_T, k, \mathbf{p})}{k} \right\} \quad (11)$$

TABLE II  
A GLOSSARY OF THE SYMBOLS USED IN THE PAPER

Group	Symbols	Meaning	Examples
Vectors	<b>Bold face</b>	Vector values.	$\mathbf{I}$ , $\mathbf{p}$ , etc
	$[\dots]^T$	Vector transpose.	
	$\  \cdot \ $	Vector length.	
Image	$\mathbf{I}$	3D Image.	
	$\mathbf{I}_{xy}, \mathbf{I}_{xz}, \mathbf{I}_{yz}$	2D images, which are obtained by projecting the 3D image onto the plane indicated by the subscript.	
	$\gamma, \sigma$	The median image intensity and its standard deviation, respectively.	
	$\mathbf{p}$	A 2D/3D image point.	
	$C$	Image contrast.	
Template	$R, L, T, B$	Right, left, top, and bottom template responses, respectively.	Eqns. 6 & 7
	$k$	The length of a template at a particular iteration.	
	$K$	The maximum template length.	
	$M$	The maximum template shift distance.	
Superscripts	$i$	Iteration number.	$\mathbf{p}^i$ in eqn. 1
	$\sim$	Approximation.	Eqn. 2.
	$\wedge$	Maximum value.	Eqns. 6 & 7.
Subscripts	$R, L, T, B$	The right, left, top, and bottom templates, respectively.	Eqns. 4, 5, 6 & 7.
	$\perp$	The orthogonal direction.	Eqns. 4 & 5.
	$I, F, B$	The image, its foreground and background, respectively.	Eqn. 16
Directions	$\mathbf{u}$	Unit direction vector	Eqn. 1 & 2.
	$\theta, \phi$	Represent the direction of a vector or template as illustrated in Figure 3(b).	
	$N$	The number of discrete directions in $\theta$ or $\phi$ producing a total of $N^2$ unique directions.	
	$s_1$	The first index of a particular direction according to $\theta = 2\pi s_1 / N$ .	Eqns. 6, 7, 10
	$s_2$	The second index of a particular direction according to $\phi = 2\pi s_2 / N$ .	Eqns. 6, 7, 10
Other	$\alpha$	The size of a tracing step.	Eqns. 1, 2
	$\Gamma$	A threshold value/function.	Eqn. 16

a local maximum, a seed-point candidate must have intensity larger than  $\gamma_{xy} + \sigma_{xy}$ , where  $\gamma_{xy}$  is the median pixel intensity of  $\mathbf{I}_{xy}$ , and  $\sigma_{xy}$  is the standard deviation around the median.

Step 2) **Filtering the Results of Step 1:** Many of the points generated in the previous step correspond to noise and must be rejected to avoid erroneous traces. For a seed-point candidate  $\mathbf{p}(x, y)$  located in the projection image  $\mathbf{I}_{xy}$ , this is achieved as follows. The *shift and correlate* procedure is applied using all *right* and *left* templates lying in the  $xy$  plane (i.e., templates with orientations  $\mathbf{u} = [s_1, 0]^T$ ,  $s_1 = 0, \dots, 31$ ). This produces a total of 64 *right* and *left* boundary points. As illustrated in Fig. 4, let  $\hat{R}_1(\mathbf{u}_{R1}, k, \mathbf{p}_{R1})$ ,  $\hat{R}_2(\mathbf{u}_{R2}, k, \mathbf{p}_{R2})$  be the two maximal right responses. Similarly, let  $\hat{L}_1(\mathbf{u}_{L1}, k, \mathbf{p}_{L1})$ ,

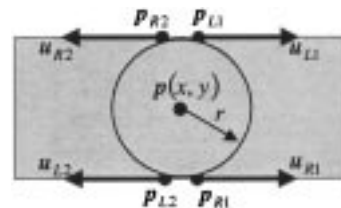


Fig. 4. Illustrating the directions and locations of the four boundary points associated with the seed-point candidate  $\mathbf{p}(x, y)$ . The circular disk of radius  $r$  is utilized in estimating the uniformity and intensity characteristics of the segment's interior.

$\hat{L}_2(\mathbf{u}_{L1}, k, \mathbf{p}_{L2})$ , be the two maximal left responses. Then we have the following conditions.

- 1)  $\mathbf{u}_{R1}$  and  $\mathbf{u}_{R2}$  must be *almost* opposite, or  $\mathbf{u}_{R1} \bullet \mathbf{u}_{R2} \leq \cos(\pi \pm 2\pi/N)$ , where “ $\bullet$ ”

indicates the inner product. A similar relation must also hold between  $\mathbf{u}_{L1}$  and  $\mathbf{u}_{L2}$ .

- 2)  $u_{R1}$  and  $u_{L1}$  must be *almost* parallel, or  $\mathbf{u}_{R1} \bullet \mathbf{u}_{L2} \leq \cos(2\pi/N)$ . A similar relation must also hold between  $\mathbf{u}_{R2}$  and  $\mathbf{u}_{L2}$ .
- 3) The segment's interior around the seed-point candidate  $p$  must be uniform. To illustrate, consider a circular disk,  $D$ , of radius  $r = (1/4)(\|\mathbf{p}_{R1} - \mathbf{p}_{R2}\| + \|\mathbf{p}_{L1} - \mathbf{p}_{L2}\|)$  centered at  $\mathbf{p}$  (see Fig. 4). Let  $\gamma_D$  be the median intensity of image pixels in  $D$ , and let  $\sigma_D$  be the standard deviation around the median. Then we have the following uniformity condition:  $\sigma_D < \sigma_{xy}$ .
- 4) The distance between  $\mathbf{p}_{R1}$  and  $\mathbf{p}_{L2}$  must be less than  $r$  pixels. Similarly, the distance between  $\mathbf{p}_{R2}$  and  $\mathbf{p}_{L1}$  must be less than  $r$  pixels.
- 5) The median intensity of the segment's interior around the seed-point candidate  $\mathbf{p}$  must be larger than that of the 2-D image  $I_{xy}$ . In terms of the disk defined above, this is stated as  $\gamma_D > (\gamma_{xy} + \sigma_{xy})$ .

Only seed-point candidates satisfying conditions 1 through 5 are considered valid. The points validated in the above procedure were obtained from the projection 2-D image  $I_{xy}$ ; hence they lie in the  $x$ - $y$  plane. The following procedure is used to estimate the  $z$  coordinates of such points to locate the corresponding 3-D seed points.

Let  $\mathbf{p}_{xy}(x_1, y_1)$  be a valid seed point. Let  $\mathbf{p}_{xyz}(x_1, y_1, z_1)$  be the corresponding 3-D seed point with the same  $x$  and  $y$  values. The value of the  $z$ -coordinate  $z_1$  is estimated as the plane with maximum local intensity in the neighborhood of  $(x_1, y_1)$ , or where a disk similar to the one defined in condition 3 above, defines the local neighborhood. Let  $\mathbf{D}(x, y, z, r)$  be a disk in the  $x$ - $y$  plane of radius  $r$  and centered at the point  $\mathbf{p}(x, y, z)$ . Denote the intensity of a 3-D image voxel by  $\mathbf{I}(x, y, z)$  and the image depth by  $Z$ . The  $z$  coordinate of the 3-D seed point is estimated according to

$$z_1 = \arg \max_{z \in \{1, \dots, Z-1\}} \sum_{\mathbf{p}(x', y', z') \in \mathbf{D}(x_1, y_1, z)} I(x', y', z'). \quad (15)$$

It is not difficult to suggest a 3-D seed selection and validation procedure instead of the hybrid 2-D/3-D procedure described above. However, such a procedure is computationally expensive. In fact, it would involve searching for local maxima along  $(N+M)Z/g$  lines, and 4096 applications of the *shift and correlate* procedure at each of the detected maxima. Compare this with the above procedure involving  $N+M$  search lines and 64 applications at each detected maxima.

To make the tracing program more robust against seed-point variations, valid seed points are ranked from *best* to *worst* according to their distance from the somas in the image (the farther the better), and according to their prominence as measured by the sum of the maximum template responses (i.e.,  $\hat{R}_1 + \hat{R}_2 + \hat{L}_1 + \hat{L}_2$ ). For other ways to prioritize seed points, the reader is referred to [34].

*Estimating Image Statistics:* Both the tracing algorithm described in Sections III-A–D and the soma detection procedure

described in Section III-F require a number of image statistics. Such statistics are gathered during this phase of processing since it takes place early on in the program. In particular, the following statistics are estimated; the median of the 3-D image  $\gamma_I$ , the median of its foreground  $\gamma_F$  (i.e., the median of all disks centered at valid seed points), the median of the background  $\gamma_B$ , and the corresponding standard deviations  $\sigma_I$ ,  $\sigma_F$  and  $\sigma_B$ , respectively. In addition, we gather statistics about the average, maximum, and minimum dendrite and axon dimensions near seed points. These measurements determine the size of the structuring element used for soma detection, as will be explained in the next section. Finally, in earlier versions of these algorithms, seed candidate validation was performed on demand while tracing. Clearly, this is computationally more attractive because of the large degree of redundancy in the number of seed points. However, this approach was abandoned in favor of the present approach because both the tracing and the soma detection algorithms depend on the estimated image statistics.

#### F. Soma Detection

Soma detection is achieved through a combination of grayscale closing, adaptive thresholding, and connected component operations. Mathematical morphology [51], [52] provides operations for enlarging, shrinking and filtering image regions in a particular grayscale range. One operation, grayscale closing, fills small gaps.<sup>1</sup> Adaptive thresholding [51] accommodates variable foreground and background regions in converting grayscale to bi-level images. Connected component analysis [51] separates foreground components from background components and provides a list of pointers to each of the latter.<sup>2</sup> However, such operations are computationally very costly if performed on the entire 3-D image. Instead, the soma detection algorithm estimates the soma projections first and then performs the above operations on the volumes defined by such projections. This is achieved as follows.

- The 3-D image is projected into the  $x$ - $y$ ,  $x$ - $z$ , and  $y$ - $z$  planes, resulting in the images,  $I_{xy}$ ,  $I_{xz}$ , and  $I_{yz}$ , respectively.
- A circular structuring element<sup>3</sup> is employed to perform a grayscale closing operation on each of the projection images. The diameter of the structuring element is adaptively set by the program to a value larger than the median width of the dendrite/axon structures present in the image. In addition, the user has the option of manually setting a lower bound on the area of detectable somas.
- The closed images are thresholded to produce a set of binary images. The threshold is set to

$$\Gamma_2 = \frac{1}{2} (\mu_F - \mu_B). \quad (16)$$

<sup>1</sup>First, all pixels within a neighborhood are replaced with the minimum pixel value in that neighborhood. Second, all pixels within a neighborhood in the resulting image are replaced with the maximum pixel value in that neighborhood.

<sup>2</sup>Connected component analysis is used for merging "connected" image regions. This is achieved by assigning all such regions the same label or pixel intensity. Two pixels are "connected" if they are adjacent. Several definitions exist for the notion of pixel adjacency.

<sup>3</sup>The structuring element is a kernel defining the neighborhood used in the closing operations.

- Finally, connected component analysis is applied to the binary images to produce a unique labeling for all soma projections.

To determine the 3-D somas, the estimated 2-D soma projections are backprojected onto the 3-D image space, therefore defining a set of intersection regions  $\chi_i$ ,  $i = 1, \dots, X$ . The above steps are then applied to all image voxels lying in such regions, with the following modifications. First, a sphere is used instead of the disk as structuring element. Second, an adaptive threshold is used instead of the one in (16), and is defined as follows. Let  $\Omega(\chi_i, z_j)$  denote the median intensity of all image voxels defined by the intersection of image plane  $z_j$  and region  $\chi_i$ . Let  $\hat{\Omega}(\chi_i, \hat{z})$  be the maximum of such medians over all planes in  $\chi_i$ . Then we have the following thresholding criterion. For all 3-D image voxels,  $I(x, y, z)$ , lying in a region  $\chi_i$ ,  $I = 1, \dots, X$ , modify them according to (17) at the bottom of the page, where  $\eta$  is empirically set to 0.95. This thresholding criterion is necessary to limit the effect of the signal from out-of-focus planes in the image (i.e., the point-spread function), which effectively cause the soma to appear larger than it is along the optical axis of the confocal microscope.

#### IV. EXPERIMENTAL RESULTS AND VALIDATION

For this study, 20 neuron images were traced. Typical examples are presented here. The brains of Wistar rats were perfusion fixed and immersion postfixed in 4% paraformaldehyde in 0.1 M phosphate buffer with 4% sucrose. Brain slices 600  $\mu\text{m}$  thick were cut on a vibratome and individual neurons were impaled with a glass micropipette and filled with Alexa 594 while being observed in an Olympus fluorescent light microscope. Slices were fixed again and resectioned at 250  $\mu\text{m}$ . The neurons were imaged using a NORAN Oz confocal attachment and the 40X (NA 1.15) water immersion lens of an Olympus IX-70 inverted infinity corrected microscope. Some images were deconvolved with NORAN's software, but validation studies revealed little benefit from deconvolution.

The tracing algorithm does not require any special hardware. The results presented here were obtained using a Pentium III 500 MHz PC, with 128 Mbytes of RAM. For a 70-Mbytes image such as the one shown in Fig. 1, it took 1.3 min. This time includes image reading and writing, soma detection, tracing, and structures creation and presentation. The actual tracing time for this image is about 30 s.

For all examples, we adjusted the contrast of the 2-D projection images for presentation purposes only. The program labels each tree emanating from the soma with a unique color and each segment is assigned a unique identifying number. These numbers can be correlated with the text-form of the program's output as will be illustrated shortly. Furthermore, the red color is reserved for segments that cannot be traced to a soma. Fig. 5 illustrates another neuron and its corresponding traces. The image has the dimensions  $512 \times 480 \times 244$ . Fig. 6 illustrates an image

of the same neuron obtained using a different field of view. The image has the dimensions  $512 \times 480 \times 281$  (i.e., 37 more slices than Fig. 5.) Figs. 1, 7, and 9 illustrate the effect of flipping and deconvolving the image on the tracing result. Fig. 7 shows a neuron image with its corresponding traces. The image in Fig. 7 was obtained by physically flipping the neuron of Fig. 1 top to bottom on the microscope stage, and then reimaging it from the opposite direction along the optical axis. Both images have the dimensions  $512 \times 480 \times 301$ . Fig. 9(a) illustrates the projections of a deconvolved version of the image in Fig. 7, and the resulting trace projections are shown in Fig. 9(b).

In addition to the trace projections, the program generates two text outputs. The first is a text representation of the somas and the traces in a format compatible with the NeuroLucida software (MicroBrightfield Inc., Colchester, VT). Incidentally, this company provides a free viewer for this file format on their web site. The second output is a text summarization of neuronal structures found in an image. An excerpt of such output is shown in Fig. 8(c). In particular, Fig. 8(c) lists soma statistics and describes the traces of the two trees identified by the red arrows in Fig. 8(b). For each tree, the program lists its root, the sum of all branch lengths, the longest path, its length, and the summed length of segments branching from it. In addition, the program lists the starting and ending points of each segment in the tree, its length, and the sum of all segments branching from such segment. Soma volume and segment lengths are given in terms of voxels, and are not corrected for the aspect ratios of a voxel.

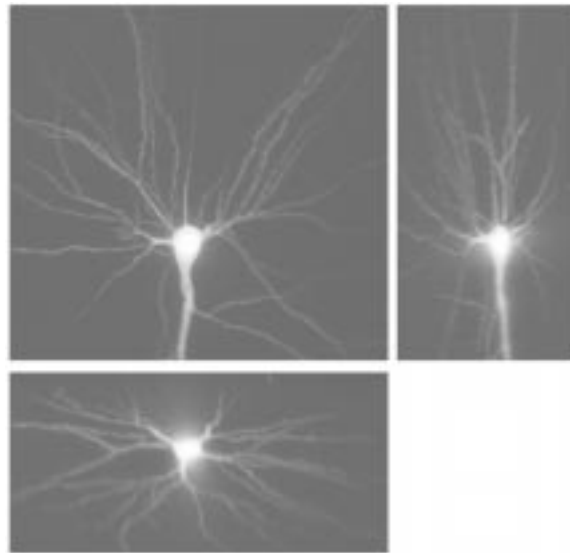
##### A. Validation of Results

From a neuroscientist's standpoint, several characteristics are important, including the centroid of a soma, its volume, its surface area, and its connectivity with other somas. In addition, it is important to determine the centerlines of all dendritic/axonal structures present, their lengths, branching point distributions, surface areas and volumes. It is also of interest to determine the topology of such structures. Clearly, quantitative evaluation of an automatic system based on these characteristics requires the availability of ground truth, which has to be established manually. In the context of 3-D neuron images such a manual process is tedious and is often ambiguous. To alleviate the effect of such ambiguity, it is necessary to have the same neuron traced by several independent experts. It is also necessary to compare the variability of the automatic system with interexpert variability. Unfortunately, such ground truth data are currently not available. This motivated a validation approach based on consistency.

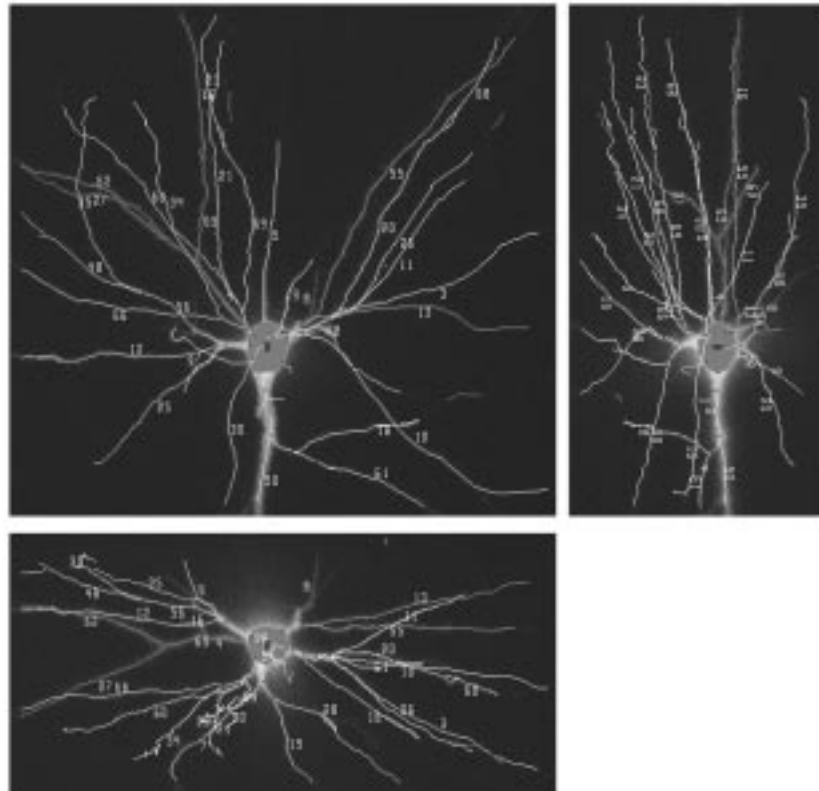
From an algorithmic point of view, a valid algorithm must be consistent. For example, if branching points are to be used as features for image registration, consistency is more important than accuracy. In this context, we define consistency as invariance under image variations. Two variations are of most interest.

**Type-1 Variations:** These arise from image transformations after the image is collected, such as translation, rotation, scale,

$$I(x, y, z) = \begin{cases} 1 & \text{if } (x, y, z) \in \chi_i \ \& \ (x, y, z) > \Gamma_2 \ \& \ \Omega(\chi_i, z) \geq \eta \hat{\Omega}(\chi_i, \hat{z}) \\ 0 & \text{otherwise.} \end{cases} \quad (17)$$



(a)



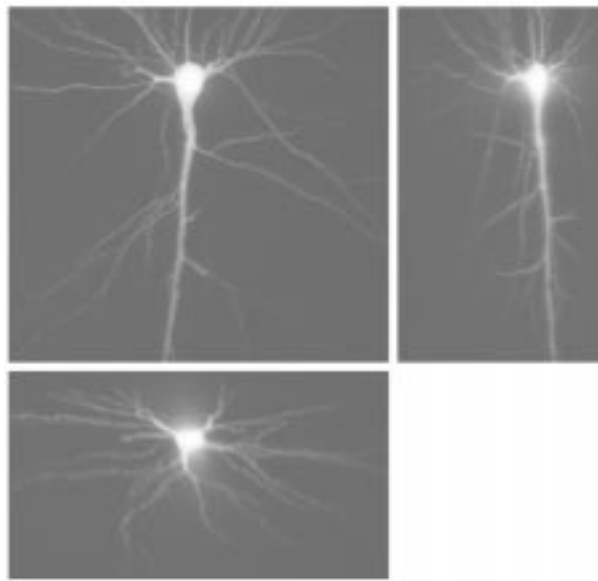
(b)

Fig. 5. (a) A different neuron imaged at a zoom of 1.0 and step size  $0.5 \mu\text{m}$ . The image dimensions are  $512 \times 481 \times 244$ . (b) Projections of the traced image, shown enlarged. Note that traces 9 and 32 are colored red because the program failed to connect them to the soma.

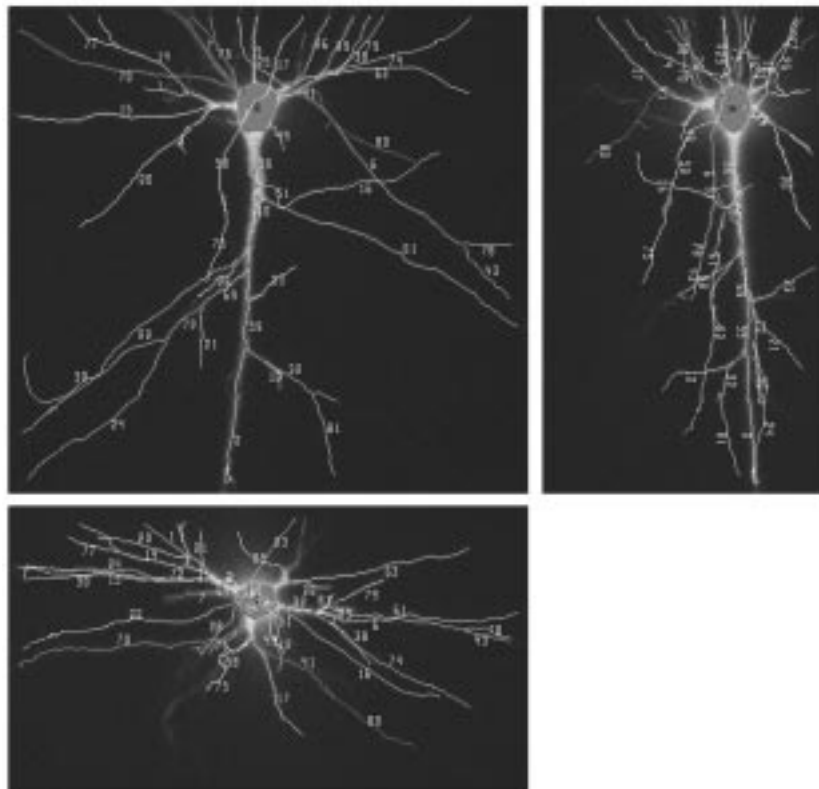
and gray-scale transformations. Figs. 7 and 8 illustrate Type-1 variations.

**Type-2 Variations:** These result from reimaging the neuron sample, either from a different view point using a different zoom, using a different step-size, with saturated/unsaturated soma or after physically flipping the specimen top-to-bottom on the microscope stage. Figs. 5 and 6, and Figs. 1 and 7 are example pairs of Type-2 variations.

Fig. 9 illustrates the consistency of the algorithm in the presence of physical image translation and variations in the gray-level values. This is demonstrated by aligning the traces of Figs. 5 and 6. Recall that the images in these two figures are different fields of view of the same neuron, and also have a different number of slices. Initial estimates for the  $X$ ,  $Y$ , and  $Z$  translations were obtained from the differences between the soma centers as estimated by the program and are given



(a)



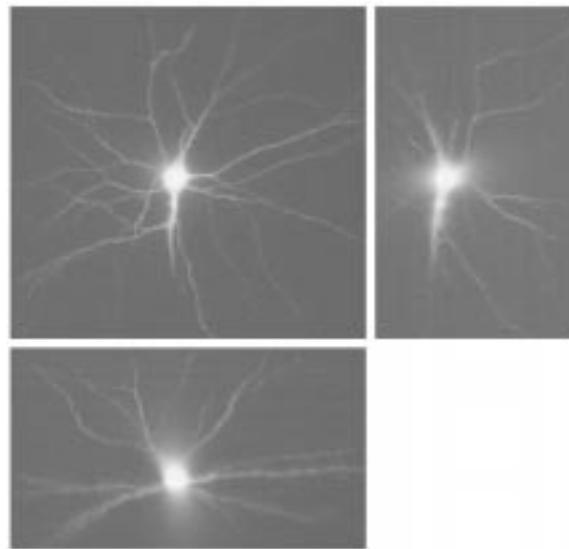
(b)

Fig. 6. The same neuron as in Fig. 5, imaged using a different field of view. (a) The projections of the 3-D neuron image. (b) The projections of the resulting traces, shown enlarged. As expected, dendrites/axons appearing in both images, are largely identical, with small differences (amounting to a mean squared error of 1.08 voxels). This is partly due to the fact that this image contains more depth information, i.e., 281 slices, compared to the image of Fig. 5.

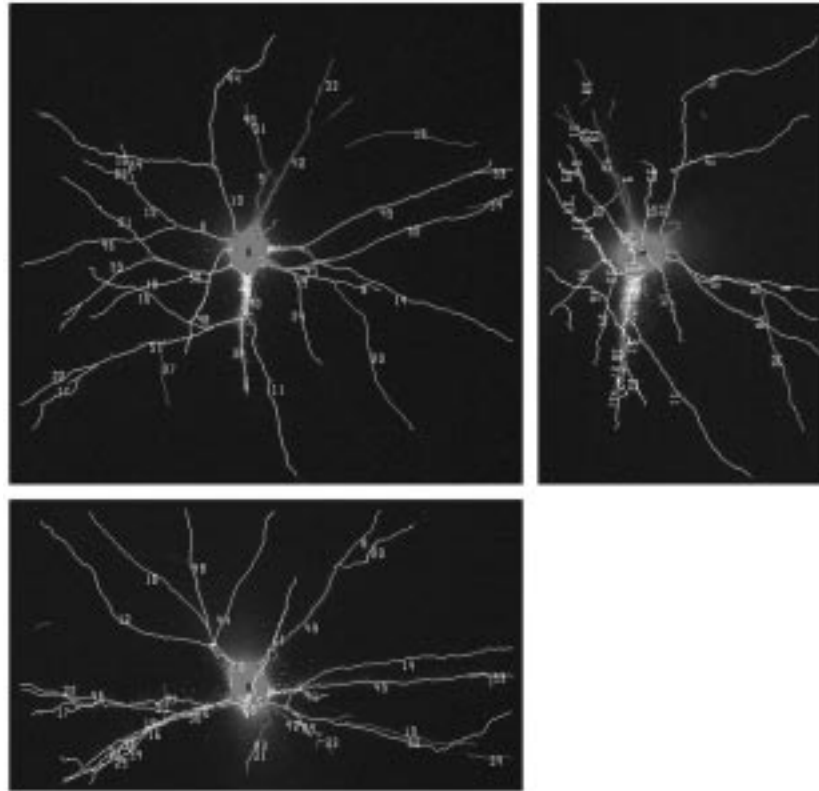
by  $[\Delta x, \Delta y, \Delta z]^T = [241, 325, 106]^T - [244, 103, 94]^T = [-3, 222, 12]^T$ . Exhaustive search was then used in the neighborhood of the initial translation estimates in order to maximize the intersection between the traces of the two images. In this particular example, the initial translation estimates were also found to be optimal. Fig. 10 illustrates the results of aligning these traces onto the field of view of each of the two images.

The mean squared error for Fig. 9(a) is 1.81 voxels, and for Fig. 9(b) is 1.63 voxels, which are typical. The figure clearly suggests a consistent tracing algorithm and focuses attention on the feasibility of constructing mosaics of 3-D neuron images.

Fig. 10 illustrates the consistency of the tracing algorithm in the presence of nonlinear image transformation. This is done by aligning the traces of Fig. 7 with those of Fig. 8. Recall that



(a)



(b)

Fig. 7. (a) This image was obtained by physically flipping the neuron of Fig. 1 under the microscope and re-imaging (zoom = 1.0, step size =  $0.5 \mu\text{m}$ ,  $512 \times 480 \times 301$ ). (b) The resulting traces. For example traces 50 and 44 correspond to traces 44 and 12 in Fig. 8, respectively. The differences are due to signal attenuation as a function of the imaging depth. This explains why some segments appear shorter (longer) in the flipped version than in the original image.

the image in Fig. 8 is a deconvolved version of that in Fig. 7, clearly a nonlinear transformation. With a mean squared error of 1.35 voxels, the tracing algorithm is very consistent in the sense that traces present in both images either coincide or are very close to each other in the aligned image. This also illustrates that expensive deconvolution does not significantly improve the results.

## V. DISCUSSION AND CONCLUSION

The present paper is a natural and complementary extension to prior work from this group [15], [16], [18]. The proposed algorithms are superior in terms of speed, automation, and robustness to skeletonization-based methods for tracing the gross neuroanatomy. If smaller structures such as spines are

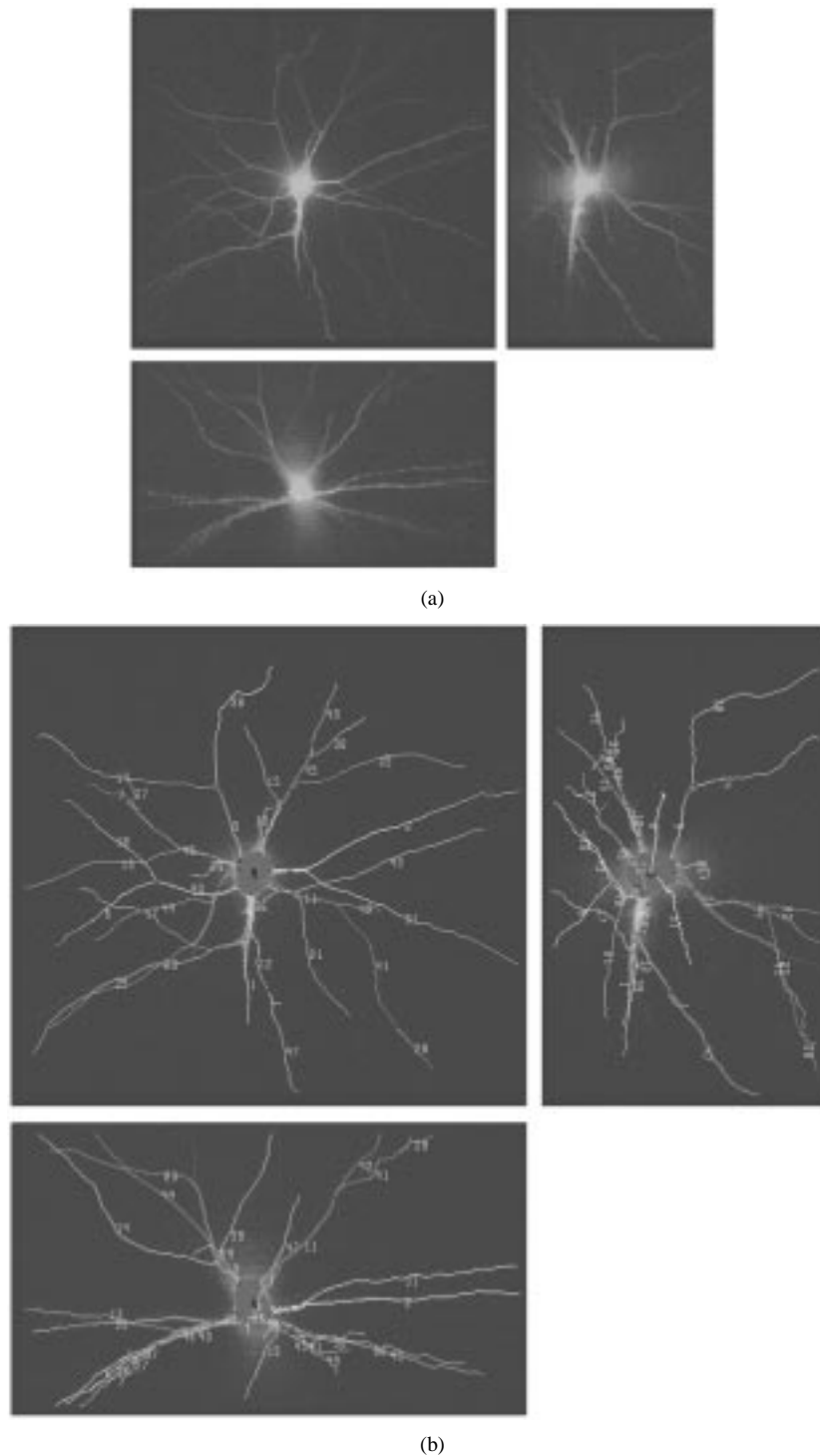


Fig. 8. (a) The result of deconvolving the image in Fig. 7. (b) The resulting traces, shown enlarged. The differences between these traces and those of Fig. 7 are minimal. For comparison, trace 14 corresponds to trace number 14 in Fig. 7, while trace 28 does not appear in Fig. 7. Overall, the algorithm appears stable to the point spread function.

also of interest, skeletonization can still be employed on a localized basis. The robustness, efficiency, and ability to work with unprocessed confocal images makes the proposed method attractive for large-scale and real-time applications such as high-throughput neuro-toxicology assays, and the Human Brain Mapping Project [53]. Also of interest are attempts to simulate computationally the electro-chemical behavior of large neuronal ensembles [54] using actual, rather than

simulated neuro-anatomical data. Of long-term interest are emerging studies of the development and growth of live neurons observed over time. Also of interest are applications beyond neurobiology. For instance, quantification of vascular changes during angiogenesis is of interest.

The algorithms have shown consistent behavior in the presence of translations, nonlinear gray-scale transformations, and imaging system variations. Such consistency is due to: 1) the

There is one soma in the image TR052Z1D

**Soma A:**

Center: 239, 247, 180  
 Volume: 42299  
 Isolated From Other Somas.  
 Hits Image Boundary? No  
 Sum Of All Branches: 4194  
 Total Of 10 Trees:

**TREE 1:**

Root: (235, 268, 190)  
 Sum Of Branches Lengths: 731  
 Longest Path: 36, 34, 8, 39  
 Length Of Longest Path: 282  
 Length Of Longest Path Branches: 449

Segment ID	From	To	Length	Branch Sum
36	(235, 268, 190)	(234, 306, 196)	40	691
12	(234, 306, 196)	(253, 365, 160)	63	236
26	(253, 365, 160)	(265, 376, 143)	28	0
47	(253, 365, 160)	(282, 465, 72)	122	0
34	(234, 306, 196)	(231, 312, 197)	8	470
8	(231, 312, 197)	(198, 323, 199)	35	349
17	(198, 323, 199)	(66, 263, 280)	150	0
39	(198, 323, 199)	(19, 427, 208)	199	0
1	(232, 397, 207)	(231, 312, 197)	86	0

**TREE 2:**

Root: (223, 259, 192)  
 Sum of Branch Lengths: 303  
 Longest Path: 40, 6  
 Length of Longest Path: 195  
 Length of Longest Path Branches: 108

Segment ID	From	To	Length	Branch Sum
40	(223, 259, 192)	(142, 256, 220)	82	221
18	(142, 256, 220)	(52, 174, 278)	108	0
6	(142, 256, 220)	(42, 318, 280)	113	0

(c)

Fig. 8. (Continued.) (c) An excerpt from the text output summarizing the traces in (b). The sample text shown here describes the soma and the traces pointed to by the arrows in the X-Y projection in (b).

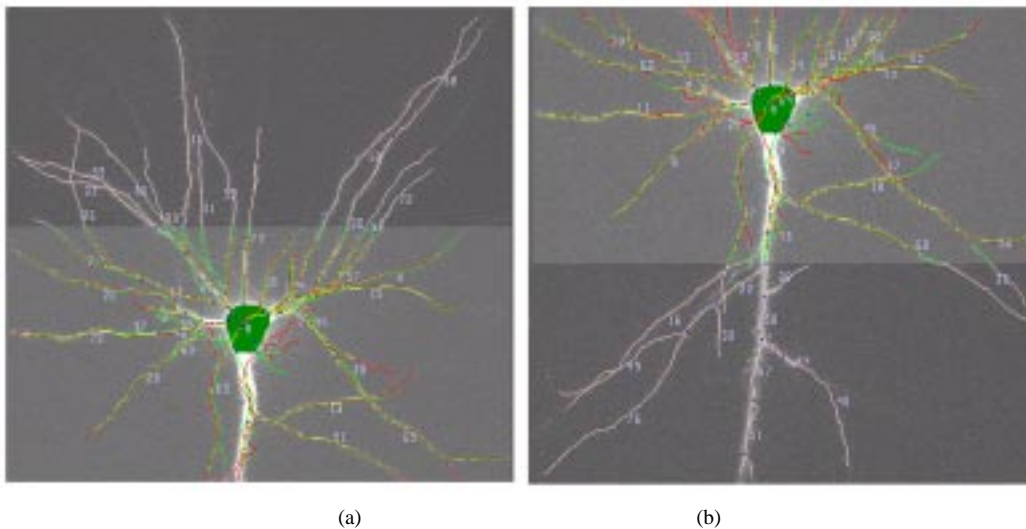


Fig. 9. Result of merging the traces from Figs. 5 and 6. (a) X-Y Projection of the combined traces into the field of view. Overlapping regions are highlighted. Segments falling outside the overlap region are colored in light Pink. Matching segments are colored in Yellow. Segments appearing in Fig. 5 only are colored in Green, and segments appearing in Fig. 7 only are colored in Red. The mean squared error is 1.63 voxels. (b) Analogous to (a), with a mean squared error of 1.63 voxels.

application of adaptive templates; 2) the use of a large number of seed points; and 3) the application of a sophisticated stop-

ping criterion. Adaptive templates allow the algorithm to trace over discontinuities in the dendrites and axons. Redundant seed

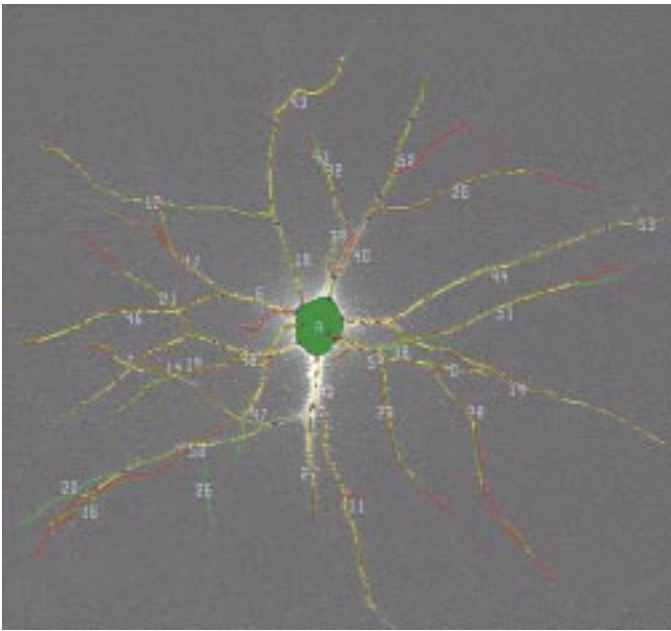


Fig. 10. The  $X$ - $Y$  projection of the merged traces from Figs. 7 and 8. Matching trace centerlines are colored in Yellow. Trace centerlines appearing in Fig. 8 only are colored in Green, and those appearing in Fig. 8 only are colored in Red. The mean squared error is 1.35 voxels.

points are necessary to ensure complete traces. In particular, if the algorithm failed to trace a segment completely, producing only a partial trace, other seed points, located on untraced parts of the same segment, will be used to provide other partial traces. The two or more partial traces are then combined to form a complete trace based on the local intensity information and the local orientations of the partial traces.

Further work is needed to quantitatively validate the algorithms against manual data. This is a difficult task given the considerations mentioned above. We leave two aspects of the algorithm for further research. The first is concerned with improving the quality of the traces, possibly by incorporating the continuity constraints of biological structure into the algorithm. Continuity constraints simply state that biological structures such as dendrites and axons or blood vessels do not undergo abrupt changes in width, direction, and intensity. In fact such constraints enabled the 2-D version of the algorithm to trace very noisy artifact-ridden 2-D neuron images.

The second aspect is concerned with a more robust stopping criterion. This is a crucial aspect of the tracing algorithm. Premature stopping results in incomplete traces, while overdue stopping results in erroneous traces. The criterion presented here improves upon prior work by using a combination of conditions, rather than a single *make or break* test. Decisions are based on the local history of the current trace. One could model the above criterion as a Markov chain with each tracing step corresponding to a state in the model. This would enable us to assign probabilities for local traces (paths). For example, the present criterion stops upon encountering a sequence of weak responses. The suggested improvement will also base its decision on how weak the responses are.

The proposed algorithms are being licensed to a commercial vendor (MicroBrightfield Inc., Colchester, VT) for user-friendly interface development and subsequent widespread dissemination.

#### ACKNOWLEDGMENT

The authors would like to thank Profs. C. V. Stewart and R. B. Kelley at Rensselaer Polytechnic Institute, for helpful discussions and advice.

#### REFERENCES

- [1] J. J. Capowski, Ed., *Computer Techniques in Neuroanatomy*. New York: Plenum, 1989.
- [2] J. D. Clements and S. J. Redman, "Cable properties of cat spinal motoneurons measured by combining voltage clamp, current clamp and intracellular staining," *J. Physiol.*, vol. 409, pp. 63–87, 1989.
- [3] S. Cullheim, J. W. Fleshman, L. L. Glenn, and R. E. Burke, "Membrane area and dendritic structure in type-identified triceps surae alpha motoneurons," *J. Comput. Neurol.*, vol. 255, pp. 68–81, 1987.
- [4] B. Ulfhake and J. O. Kellerth, "Electrophysiological and morphological measurements in cat gastrocnemius and soleus—motoneurons," *Brain Res.*, vol. 307, pp. 167–179, 1984.
- [5] B. Ulfhake and S. Cullheim, "A quantitative light microscopic study of the dendrites of cat spinal  $\alpha$ -motoneurons after intracellular staining with horseradish peroxidase," *J. Comput. Neurol.*, vol. 202, pp. 585–596, 1981.
- [6] G. Simic, I. Kostovic, B. Winblad, and N. Bogdanovic, "Volume and neuron numbers of the human hippocampal formation in normal aging and Alzheimer's disease," *J. Comput. Neurol.*, vol. 379, pp. 482–494.
- [7] J. A. Mong, E. Glaser, and M. M. McCarthy, "Gonadal steroids promote glial differentiation and alter neuronal morphology in the developing hypothalamus in a regionally specific manner," *J. Neurosci.*, vol. 19, pp. 1464–1472, 1999.
- [8] B. Willis, B. Roysam, J. N. Turner, and T. J. Holmes, "Iterative, constrained 3-D image reconstruction of transmitted light bright-field micrographs based on maximum-likelihood reconstruction," *J. Microscopy*, pt. 3, vol. 169, pp. 347–361, March 1993.
- [9] J. N. Turner, W. Shain, D. H. Szarowski, S. Lasek, B. Sipple, C. Pace, K. Al-Kofahi, A. Can, and B. Roysam, "Confocal light microscopy of brain cells and tissue: Image analysis & quantitation," *Acta Histochemica et Cytochemica*, vol. 32, no. 1, pp. 5–11, 1999.
- [10] T. J. Holmes, S. Bhattacharyya, J. A. Cooper, D. Hanzel, V. Krishnamurthi, W. Lin, B. Roysam, D. H. Szarowski, and J. N. Turner, "Light microscopic images reconstructed by maximum likelihood deconvolution," in *Handbook of Confocal Microscopy*, J. Pawley, Ed. New York: Plenum, 1995.
- [11] J. N. Turner, D. H. Szarowski, K. L. Smith, M. Marko, A. Leith, and J. W. Swann, "Confocal microscopy and three-dimensional reconstruction of electrophysiologically identified neurons in thick brain slices," *J. Electron Microscopy Tech.*, vol. 18, pp. 11–23, 1991.
- [12] C. F. Garvey, J. Young, W. Simon, and P. D. Coleman, "Automated three-dimensional dendrite tracking system," *Electroencephalogr. Clin. Neurophysiol.*, vol. 35, pp. 199–204, 1973.
- [13] P. D. Coleman, C. F. Garvey, J. Young, and W. Simon, "Semiautomated tracing of neuronal processes," in *Computer Analysis of Neuronal Structures*, R. D. Lindsay, Ed. New York: Plenum, 1977, pp. 91–109.
- [14] J. R. Glaser and E. Glaser, "Neuron imaging with neurolucida—A PC-based system for image combining microscopy," *Comput. Med. Imaging Graphics*, vol. 14, pp. 307–317, 1990.
- [15] A. R. Cohen, B. Roysam, and J. N. Turner, "Automated tracing and volume measurements of neurons from 3-D confocal fluorescence microscopy data," *J. Microscopy*, vol. 173, no. 2, pp. 103–114, 1994.
- [16] W. He, A. R. Cohen, J. N. Turner, T. J. Holmes, and B. Roysam, "Adaptive 3-D skeletonization of noisy images using  $N \times N \times N$  connectivity analysis windows and robust surface detection," *IEEE Trans. Inform. Technol. Biomed.*, to be published.
- [17] W. He, T. A. Hamilton, A. R. Cohen, T. J. Holmes, J. N. Turner, and B. Roysam, "Automated three-dimensional tracing of hrp stained neurons from a stack of brightfield optical slices," *Microscopy Microanal.*, to be published.
- [18] A. Can, H. Shen, J. N. Turner, H. L. Tanenbaum, and B. Roysam, "Rapid automated tracing and feature extraction from retinal fundus images using direct exploratory algorithms," *IEEE Trans. Inform. Technol. Biomed.*, vol. 3, pp. 125–138, June 1999.

- [19] M. H. Goldbaum, N. Katz, S. Chaudhuri, M. Nelson, and P. Kube, "Digital image processing for ocular fundus images," *Ophthalmol. Clin. N. Amer.*, vol. 3, no. 3, pp. 447–466, 1990.
- [20] M. H. Goldbaum, V. Kouznetsova, B. L. Cote', W. E. Hart, and M. Nelson, "Automated registration of digital ocular fundus images for comparison of lesions," *SPIE: Ophthalmic Technologies III*, vol. 1877, pp. 94–99, 1993.
- [21] T. M. Clark, W. R. Freeman, and M. H. Goldbaum, "Digital overlay of fluorescein angiograms and fundus images for treatment of subretinal neovascularization," *Retina-J. Retinal Vitreous Diseases*, vol. 2, no. 12, pp. 118–126, 1992.
- [22] S. Chaudhuri, S. Chatterjee, N. Katz, M. Nelson, and M. Goldbaum, "Detection of blood vessels in retinal images using two-dimensional matched filters," *IEEE Trans. Med. Imag.*, vol. 8, pp. 263–269, 1989.
- [23] R. Polli and G. Valli, "An algorithm for real-time vessel enhancement and detection," *Comput. Meth. Programs Biomed.*, vol. 52, pp. 1–22, 1997.
- [24] M. Sonka, M. D. Winniford, and S. M. Collins, "Reduction of failure rates in automated analysis of difficult images: Improved simultaneous detection of left and right coronary borders," *Comput. Cardiol.*, pp. 111–114, 1992.
- [25] M. Sonka, M. D. Winniford, X. Zhang, and S. M. Collins, "Lumen centerline detection in complex coronary angiograms," *IEEE Trans. Med. Imag.*, vol. 41, pp. 520–528, 1994.
- [26] M. Sonka, M. D. Winniford, and S. M. Collins, "Coronary borders in complex images," *IEEE Trans. Med. Imag.*, vol. 14, pp. 151–161, 1995.
- [27] P. H. Eichel, E. J. Delp, K. Koral, and A. J. Buda, "A method for a fully automatic definition of coronary arterial edges from cineangiograms," *IEEE Trans. Med. Imag.*, vol. 7, pp. 313–320, 1988.
- [28] M. A. Figueiredo and M. N. Leitao, "A nonsmoothing approach to estimation of vessel contours in angiograms," *IEEE Trans. Med. Imag.*, vol. 14, pp. 162–172, 1995.
- [29] R. Kutka and S. Stier, "Extraction of line properties based on direction fields," *IEEE Trans. Med. Imag.*, vol. 15, pp. 51–58, 1996.
- [30] D. P. Kottke and Y. Sun, "Segmentation of coronary arteriograms by iterative ternary classification," *IEEE Trans. Biomed. Eng.*, vol. 37, pp. 778–785, 1990.
- [31] P. M. J. Zwet and P. M. J. Reiber, "A new algorithm to detect coronary boundaries: the gradient field transform," *Comput. Cardiol.*, pp. 107–110, 1992.
- [32] J. L. Coatrieux, M. Garreau, R. Collorec, and C. Roux, "Computer vision approaches for the three-dimensional reconstruction: Review and prospects," *Critical Rev. Biomed. Eng.*, vol. 22, no. 1, pp. 1–38, 1994.
- [33] R. D. T. Janssen and A. M. Vossepoel, "Adaptive vectorization of line drawing images," *Comput. Vision Image Understanding*, vol. 65, no. 1, pp. 38–56, 1997.
- [34] H. Shen, B. Roysam, C. V. Stewart, J. N. Turner, and H. L. Tanenbaum, "Optimal scheduling of tracing computations for real-time vascular landmark extraction from retinal fundus images," *IEEE Trans. Inform. Technol. Biomed.*, vol. 5, Mar. 2001.
- [35] M. S. Zhou, L. J. Rzeszutowski, Singerman, and J. M. Chokreff, "The detection and quantification of retinopathy using digital angiograms," *IEEE Trans. Med. Imag.*, vol. 13, pp. 619–626, 1994.
- [36] Y. Sun, "Automated identification of vessel contours in coronary arteriograms by an adaptive tracking algorithm," *IEEE Trans. Med. Imag.*, vol. 8, pp. 78–88, 1989.
- [37] Y. Sun, R. J. Lucariello, and S. A. Chiamarida, "Directional low-pass filtering for improved accuracy and reproducibility of stenosis quantification in coronary arteriograms," *IEEE Trans. Med. Imag.*, vol. 14, pp. 242–248, 1995.
- [38] J. H. Van Cuyck, J. J. Gerbrands, and J. H. C. Reiber, "Automated centerline tracing in coronary angiograms," *Pattern Recogn. Artificial Intell.*, pp. 169–183, 1998.
- [39] A. Klein, T. K. Egglin, J. S. Pollak, F. Lee, and A. A. Amini, "Identifying vascular features with orientation specific filters and B-spline snakes," *Comput. Cardiol.*, pp. 113–116, 1994.
- [40] M. Hart and L. Holly, "A method of automated coronary tracking in unsubtracted angiograms," *Comput. Cardiology*, pp. 93–96, 1993.
- [41] E. Mortensen, B. Morse, W. Barrett, and J. Udupa, "Adaptive boundary detection using live-wire two-dimensional dynamic programming," *Comput. Cardiology*, pp. 635–638, 1992.
- [42] L. Van Tran, R. C. Bahn, and J. Sklansky, "Reconstructing the cross sections of coronary arteries from biplane angiograms," *IEEE Trans. Med. Imag.*, vol. 11, pp. 517–529, 1992.
- [43] T. N. Pappas and J. S. Lim, "A new method for estimation of coronary artery dimensions in angiograms," *IEEE Trans. Acoust., Speech, Signal Processing*, vol. 36, pp. 1501–1513, 1988.
- [44] I. Liu and Y. Sun, "Recursive tracking of vascular networks in angiograms based on detection-deletion scheme," *IEEE Trans. Med. Imag.*, vol. 12, pp. 334–341, 1993.
- [45] S. Lu and S. Eiho, "Automated detection of the coronary arterial contours with sub-branches from an X-ray angiogram," *Comput. Cardiol.*, pp. 575–578, 1993.
- [46] K. Kitamura, J. M. Tobis, and J. Sklansky, "Estimating the X-ray intercepted areas and boundaries of coronary arteries," in *Proc. Int. Conf. Pattern Recogn.*, Paris, France, 1986, pp. 478–480.
- [47] M. Garreau and J. L. Coatrieux *et al.*, "A knowledge-based approach for 3-D reconstruction and labeling of vascular networks from biplane angiographic projections," *IEEE Trans. Med. Imag.*, vol. 10, pp. 122–131, 1991.
- [48] T. V. Nguyen and J. Sklansky, "Computing the skeleton of coronary arteries in cineangiograms," *Comput. Biomed. Res.*, vol. 19, pp. 428–444, 1986.
- [49] J. B. Pawley, Ed., *Handbook of Biological Confocal Microscopy*. New York: Plenum, 1995.
- [50] B. Matsumoto, Ed., "Cell biology applications of confocal microscopy," in *Methods in Cell Biology*. New York: Academic, 1993, vol. 38.
- [51] R. M. Haralick and L. G. Shapiro, *Computer and Robot Vision*. New York: Addison-Wesley, 1992, vol. 1.
- [52] L. Vincent, "Morphological algorithms," in *Math. Morphology in Image Processing*, E. Dougherty, Ed. New York: Marcel-Dekker, 1992, pp. 255–288.
- [53] *Neuroinformatics: An Overview of the Human Brain Project*, S. H. Koslow and M. F. Huerta, Eds., Lawrence Erlbaum, Mahwah, NJ, 1997.
- [54] S. L. Senft and T. A. Woolsey, "Computer-aided analyzes of thalamocortical afferent ingrowth," *Cereb. Cortex*, vol. 1, no. 4, pp. 336–47, 1991.



**Khalid A. Al-Kofahi** received the B.Sc. degree in electrical and computer engineering from Jordan University of Science and Technology (JUST), Irbid, Jordan, in 1989, the M.Sc. degree in computer engineering from Rochester Institute of Technology (RIT), Rochester, NY, in 1993, and the Ph.D. degree in computer and systems engineering from Rensselaer Polytechnic Institute (RPI), Troy, NY, in 2000.

Since 1995, he has been with the Research and Development Department of Thomson Legal and Regulatory, Rochester, NY. His research interests include 2-D and 3-D image processing and analysis, computer vision, information extraction, retrieval and classification, natural language processing, and machine learning.

Dr. Al-Kofahi is the recipient of the 2001 Allen B. DuMont award for scholastic achievements from Rensselaer.



**Sharie Lasek** received the B.S. degree in molecular biology and preprofessional biology from the Florida Institute of Technology, Melbourne, in 1997.

Since 1997, she has been with the Wadsworth Center for Laboratories and Research, New York State Department of Health, Albany, where she is currently a Senior Technician. She handles daily operations of the Three-Dimensional Light Microscopy Facility at the Wadsworth Center and is also involved with the Neuro-Prosthesis Research Project.



**Donald H. Szarowski** received the B.S. degree in biology from the State University of New York at Fredonia, Fredonia, in 1969.

He has been a Research Assistant with the Worcester Foundation for Experimental Biology, Shrewsbury, MA, New York Medical College, New York, and Albany Medical College, Albany, NY. He is currently a Research Scientist at the Wadsworth Center for Laboratories and Research, New York State Department of Health, Albany, NY, where he is the supervisor of the Three-Dimensional Light

Microscopy Facility.



**Christopher J. Pace** received the B.S. degree in biological sciences and the Ph.D. degree in neuroscience from the State University of New York at Albany, Albany, in 1992 and 2001 respectively.

He currently has a temporary faculty appointment in the Department of Biological Sciences and is working as a Research Assistant with the Center for Neuroscience Research at the State University of New York at Albany. He has also been a research assistant at the Wadsworth Center for Laboratories and Research, New York State Department of Health and as a Research Consultant with BioQuant Inc. His interests include the development and plasticity of the nervous system. In particular, he is interested in how individual cells within the brain take their characteristic shape and to what extent this shape relates to function. As such, his dissertation research focused on the detailed structure of nerve cells and to what extent sensory experience participates in the development of this structure.



**George Nagy** (M'66–SM'72) received the B.Eng. and M.Eng. degrees from McGill University, Montreal, QC, Canada, and the Ph.D. degree in electrical engineering on neural networks from Cornell University, Ithaca, NY, in 1962.

For the next ten years, he conducted research on various aspects of pattern recognition and OCR at the IBM T.J. Watson Research Center, Yorktown Heights, NY. From 1972 to 1985, he was Professor of computer science at the University of Nebraska–Lincoln, Lincoln, and worked on remote sensing applications, geographic information systems, computational geometry, and human-computer computer interfaces. Since 1985, he has been Professor of computer engineering at Rensselaer Polytechnic Institute, Troy, NY. He has held visiting appointments at the Stanford Research Institute, Cornell, McGill, the Universities of Montreal, Genoa, Uppsala and Bern, the National Scientific Research Institute of Quebec, the Italian National Research Council in Naples and Genoa, AT&T Bell Laboratories, IBM Almaden, and the Institute for Information Science Research at the University of Nevada. In addition to computer vision, document image analysis and character recognition, his interests include solid modeling and finite-precision spatial computation.



**James N. Turner** received the B.S. degree in engineering science and the Ph.D. degree in biophysics from the State University of New York at Buffalo, Buffalo, in 1968 and 1973, respectively.

He did National Institutes of Health and National Science Foundation Postdoctoral Fellowships at the Roswell Park Memorial Institute, Buffalo. Currently, he is Director of the Three-Dimensional Light Microscopy Facility and the Nanobiotechnology Program at the Wadsworth Center of the New York State Department of Health, Albany, and a Platform Leader and Executive Committee Member of the Nanobiotechnology Center, an NSF sponsored Science and Technology Center lead by Cornell University. He is Professor of biomedical engineering at Rensselaer Polytechnic Institute and of Biomedical Sciences in the School of Public Health of the University at Albany. He is interested in applications of light imaging methods and quantitative image analysis in biology and medicine with a special emphasis on the nervous system. He is on the editorial board of *Microscopy and Microanalysis*.

Dr. Turner has chaired numerous symposia in the area of 3-D microscopy, both light and electron, at national meetings. He is a member of the Microscopy Society of America, International Society for Analytical Cytology, and the Society for Neuroscience. He frequently serves on NIH advisory panels.



**Badrinath Roysam** (M'89) received the B.Tech degree in electronics engineering from the Indian Institute of Technology, Madras, India, in 1984, and the M.S. and D.Sc. degrees from Washington University, St. Louis, MO, in 1987, and 1989, respectively.

Since 1989, he has been with Rensselaer Polytechnic Institute, Troy, NY, where he is currently Professor in the Electrical, Computer, and Systems Engineering Department. He also holds an appointment in the Biomedical Engineering Department. His ongoing projects are in the areas of 2-D, 3-D, and 4-D biomedical image analysis, biotechnology automation, optical instrumentation, high-speed and real-time computing architectures, and parallel algorithms.

Dr. Roysam is a corecipient of the Best Paper Award at the 1999 IEEE Conference on Computer Vision and Pattern Recognition (CVPR). He is an Associate eEditor for the IEEE TRANSACTIONS ON INFORMATION TECHNOLOGY IN BIOMEDICINE. He is a member of the Microscopy Society of America, the Society for Neuroscience, and the Association for Research in Vision and Ophthalmology.